SHADOW-AWARE NONLINEAR SPECTRAL UNMIXING WITH SPATIAL REGULARIZATION

Guichen Zhang, Daniele Cerra, Rupert Müller

German Aerospace Center (DLR)
Remote Sensing Technology Institute (IMF)
82234 Wessling, Germany

Paul Scheunders

University of Antwerp, Campus CDE
Imec-Visionlab, Department of Physics
2610, Wilrijk, Belgium

ABSTRACT

This paper presents a nonlinear spectral unmixing method jointly considering shadow effect and spatial relationships in local neighborhoods. Sunlit and shadowed spectra are modeled by considering two illumination sources, i.e., direct and diffuse solar radiation. Specifically, we model the spectrum of a material in shadowed regions according to the spectrum of the same material exposed to direct sunlight. Furthermore, we embed a weighted total variation regularization in order to keep the spatial relationships among pixels. Weighting factors take into account the similarity of neighboring pixels by considering the spectral information from the hyperspectral imagery, height information from the image-generated digital surface model (DSM), and shadow effects. The optimization problem is solved by the Alternating Direction Method of Multipliers (ADMM). Experimental results demonstrate that the proposed shadow-aware unmixing method performs better with the aid of the spatial regularization.

Index Terms— Spectral unmixing, shadow, spatial regularization, digital surface model (DSM), HySpex

1. INTRODUCTION

Spectral unmixing methods decompose mixed hyperspectral pixels into spectral signatures of ground materials, i.e., endmembers, along with their corresponding contributions, i.e., abundances [1, 2, 3]. In the past decades, numerous spectral mixing models have been developed, which simplify the real optical interactions to certain degrees with or without physical interpretations [1, 2, 3]. The most common model is the linear mixing model (LMM) [1], but nonlinear models have attracted lots of attentions in the past decades. One group of models regard nonlinear optical interactions up to the second order. Depending on their assumptions, different types of models have been proposed, such as the Nascimento model, the Fan model, and the GBM (Generalized Bilinear Model) [1]. Some works extended the nonlinear optical interactions to unlimited orders [4, 5].

For the sake of spectral modeling, the shadow effect has also attracted attention. One category of models regards shadow as a wavelength-independent scaling effect [6, 7] that can be by either adding a "zero-reflectance" spectrum or including a scaling parameter into the mixture models. Another category of models regards shadow as a wavelength-dependent effect by considering multiple illumination sources, i.e. sunlight and skylight, thus achieving better spectral representations [8, 9]. Due to low signal-to-noise ratio in shadowed regions, the unmixing results exhibit higher noise when including the skylight information [8]. In addition, including the skylight can lead to inaccurate abundance results in the shadowed regions of complex scenes, causing unnatural transitions in shadow boundaries [8].

Next to modeling of the spectral information, embedding spatial information has attracted research interest in spectral unmixing [10, 11]. One popular group of methods applies spatial regularization to the spectral mixing models in order to promote spatial homogeneity among pixels in a local neighborhood. In [11], authors embed total variation (TV) regularization into the LMM, aiming to minimize the abundance differences between a target pixel and its first order neighboring pixels, which largely improves the spatial correlation of abundance values. In order to preserve the edges in the image, later works added weighting parameters to the TV-regularization terms. The weights account for the spectral similarity between pixels [12, 13]. When additional height data is available, regularization with respect to height similarity can be performed, which is advantageous for scenes with high spectral variability, as height data is invariant to ilumination conditions.

Following our previous work in [8], we first introduce a shadow-aware nonlinear spectral mixing model based on physical assumptions. Then we embed spatial regularization in the spectral mixing model using a weighted total variation (TV) regularizer, where the weighting factors are derived by jointly considering spectral, height and shadow information. Specifically, the height information is provided by an image-generated digital surface model (DSM). Furthermore, the nonlinear optimization is then constructed as a bi-convex problem and solved by the ADMM (Alternating Direction Method of Multipliers) [14].

2. METHODOLOGY

According to our previous work in [8], we present a shadow-aware spectral mixing model, considering shadow effects in a wavelength dependent manner. The motivation is to improve the spectral modeling in shadowed regions to better represent ground mixtures at different illumination conditions. We consider both direct and diffuse solar illuminations, assuming that fully sunlit pixels receive both direct and diffuse solar illuminations and fully shadowed pixels receive solely the diffuse solar illumination. Given the spectrum of a material $r(\lambda)$ exposed to direct solar illumination, we model the spectra $r_s(\lambda)$ of the same material in a fully shadowed region as:

$$r_s(\lambda) = \frac{F \cdot (k_1 \lambda^{-k_2} + k_3)}{1 + F \cdot (k_1 \lambda^{-k_2} + k_3)} \cdot r(\lambda) \qquad (1)$$

The wavelength-dependent fractional term models the proportion of the diffuse solar illumination with respect to the global solar illumination, using a power function $(k_1 \lambda^{-k_2} + k_3)$ with $k_1, k_2, k_3 \geq 0$. If no occlusion occurs on a ground pixel, the diffuse radiation comes from all directions of the sky. Otherwise, the diffuse illumination decreases by the sky view factor $F \in [0, 1]$, representing the fraction of sky that a ground pixel can "see". In this paper, F is computed using DSM data, generated from the images [15] using the software SAGA GIS [16]. Despite the fact that the image-generated DSM has lower accuracy compared to a Lidar-generated DSM, it is sufficient for our application and provides valuable information when Lidar data are not available.

Given that a pixel can contain several materials and is often partially shadowed in a real scenario, we use a parameter Q to represent the fraction of shadow within a pixel. Furthermore, we model multiple reflections from neighboring pixels to the target pixel up to the second order. The proposed spectral mixing model for pixel j is give by:

$$\begin{aligned} \boldsymbol{x_j} = &(1 - Q_j) \sum_{i=1}^{p} a_{j,i} \boldsymbol{e_i} + Q_j \sum_{i=1}^{p} a_{j,i} \boldsymbol{e_i} \cdot \widetilde{\boldsymbol{F_j}} + \\ &K_j \sum_{i=1}^{p} \boldsymbol{e_i} \cdot \boldsymbol{e_{N_j}} \end{aligned} \qquad (2)$$

The three terms represent three types of contributions, i.e., sunlit, shadowed and nonlinear interactions for a pixel j. $\widetilde{\boldsymbol{F_j}} = \frac{F_j \cdot (k_1 \boldsymbol{\lambda}^{-k_2} + k_3)}{1 + F_j \cdot (k_1 \boldsymbol{\lambda}^{-k_2} + k_3)}$, $\{\boldsymbol{e_i}\}_{i=1}^{p}$ are the endmembers and $a_{j,i}$ is the abundance value of endmember i at pixel j, and p is the total number of endmembers. $\boldsymbol{e_{N_j}}$ is the mean spectrum of neighboring pixels of the target pixel j, while K is the fraction of the multiple reflections from the neighboring pixels that the pixel receives.

Note that $\boldsymbol{X} = [\boldsymbol{x_1}, \boldsymbol{x_2}, \cdots, \boldsymbol{x_N}]$, where $\boldsymbol{x_j} \in R^{L \times 1}$. $\boldsymbol{E} = [\boldsymbol{e_1}, \boldsymbol{e_2}, \cdots, \boldsymbol{e_p}]$. $\boldsymbol{A} = [\boldsymbol{a_1}, \boldsymbol{a_2}, \cdots, \boldsymbol{a_N}]$, where $\boldsymbol{a_j} \in R^{p \times 1}$. $\boldsymbol{K} = [K_1, K_2, \cdots, K_N]$, $\boldsymbol{F} = [F_1, F_2, \cdots, F_N]$,

$\boldsymbol{e_N} = [\boldsymbol{e_{N_1}}, \boldsymbol{e_{N_2}}, \cdots, \boldsymbol{e_{N_N}}]$, where N is the number of pixels. We construct the optimization problem as:

$$\min_{\boldsymbol{A}, \boldsymbol{Q}, \boldsymbol{K}} \frac{1}{2} \sum_{j=1}^{N} \|\widetilde{\boldsymbol{E}_j} \boldsymbol{A_j} - \boldsymbol{X_j}\|_F^2 \qquad (3)$$

where

$$\widetilde{\boldsymbol{E}_j} = \boldsymbol{E} \odot ((\mathbf{1}_L - \mathbf{1}_L Q_j + \widetilde{\boldsymbol{F}_j} Q_j + \boldsymbol{e_{N_j}} K_j) \mathbf{1}_p^T) \qquad (4)$$

Following several previous works, we apply the ANC (abundance non-negativity constraint) and ASC (abundance sum-to-one constraint) on the abundance values $\boldsymbol{a_j}$. Additionally, we assume Q and $K \in [0, 1]$, in order to keep their physical meanings:

$$\boldsymbol{a_j} \geq 0, \sum_{i=1}^{p} \boldsymbol{a_{j,i}} = 1, Q, K \in [0, 1] \qquad (5)$$

Inspired by existing works on weighted total variation constraints for spectral unmixing [13, 12], the spatial constraint is described as:

$$\sum_{j=1}^{N} \sum_{m \in \mathcal{N}(j)} R_{j,m} \|\boldsymbol{a_j} - \boldsymbol{a_m}\|_1^1 \qquad (6)$$

where $\mathcal{N}(j)$ denotes the first order neighboring pixels of the target pixel j, and $R_{j,m}$ a weighting factor, describing the similarity between pixel j and m, based on both spectral and height information. In this paper, we use two exponential functions to describe the spectral and height similarities between target pixel j and its neighboring pixel m. The smaller the spectral and height distance to the target pixel j, the larger the exponential functions become (see Eq. (7)), thus the constraint encourages m to have similar abundances with the target pixel j.

To measure the spectral similarity, accounting for shadow effects, we use the spectral angle. The height information from the DSM data provides illumination-insensitive information. Furthermore, as abundance values in shadowed regions can not be estimated as accurately as those in sunlit regions, and often exhibit a higher noise level caused by the low signal-to-noise ratio in shadowed areas [8], we embed the pre-calculated shadow-related factor $1 - Q'_{j,m}$, by which the sunlit neighboring pixels have more impact to the target pixel than shadowed neighboring pixels. For a target pixel j, the weighting factor from its neighboring pixel m can then be computed as:

$$\begin{aligned} R_{j,m} = &\frac{1}{Z_j} \left\{ (1 - Q'_{j,m}) \left[exp \left(-\frac{1}{\delta_x^2} \arccos \frac{\boldsymbol{x}_j \cdot \boldsymbol{x}_m}{\|\boldsymbol{x}_j\| \|\boldsymbol{x}_m\|} \right) + \right. \right. \\ &\left. \left. exp \left(-\frac{1}{\delta_h^2} \frac{(h_j - h_m)^2}{(h_j + h_m)^2} \right) \right] \right\} \end{aligned}$$

$$(7)$$

where $Q'_{j,m}$ is the pre-calculated shadow fractional value through the method in [8], h and x are the height and reflectance, respectively. Z_j is the normalizing constant value, δ_x^2 and δ_h^2 are the constant parameters of the exponential functions controlling the weight range.

In this paper, we apply the weighted TV regularization to A. In addition, we apply a non-weighted TV regularization to K, because nonlinear effects are generally not dependent the spectral, height, and shadow conditions. Hence, we write the optimization problem with spectral and spatial constraints as follows:

$$\min_{A,Q,K} \frac{1}{2} \sum_{j=1}^{N} \|\widetilde{E_j} A_j - X_j\|_F^2 + \lambda\|AW_1\|_{1,1} + \ell_{\mathcal{N}}(A) + $$
$$\ell_{\mathcal{S}}(A) + \ell_{\mathcal{M}}(Q) + \lambda\|KW_2\|_{1,1} + \ell_{\mathcal{M}}(K) \tag{8}$$

where $\ell_{\mathcal{N}}(A) = \{A | A \geq \mathbf{0}_{p\times N}\}$, $\ell_{\mathcal{S}}(A) = \{A | \mathbf{1}_p^T A = \mathbf{1}_N^T\}$, $\ell_{\mathcal{M}}(Q) = \{Q | Q \geq \mathbf{0}_{1\times N}, Q \leq \mathbf{1}_{1\times N}\}$, $\ell_{\mathcal{M}}(K) = \{K | K \geq \mathbf{0}_{1\times N}, K \leq \mathbf{1}_{1\times N}\}$, $W_1 \in R^{N\times 4N}$ computes the differences between a target pixel j and its neighboring pixels weighted by the factor $R_{j,m}$, $W_2 \in R^{N\times 4N}$ computes the differences between a target pixel j and its neighboring pixels without weighting factors.

The above optimization is a bi-convex problem, and it is convex with respect to A and $\{Q, K\}$, respectively. Following many successful applications to such problems [14, 17], we split the unknown variables into two groups and solve two convex problems sequentially through ADMM. We write the optimization into the ADMM form in Eq. ((9)). The detailed updating sequence is reported in Algorithm 1.

$$\min_{A,Q,K,G,H} \frac{1}{2} \sum_{j=1}^{N} \|\widetilde{E_j} A_j - X_j\|_F^2 + \lambda\|G_2\|_{1,1} + $$
$$\ell_{\mathcal{N}}(G_3) + \ell_{\mathcal{S}}(G_4) + \ell_{\mathcal{M}}(H_1) + \lambda\|H_3\|_{1,1} + \ell_{\mathcal{M}}(H_4)$$
$$s.t.\ G_1 = A, G_2 = G_1 W_1, G_3 = A, G_4 = A, H_1 = Q,$$
$$H_2 = K, H_3 = H_2 W_2, H_4 = K. \tag{9}$$

with $G = [G_1, G_2, G_3, G_4]$ and $H = [H_1, H_2, H_3, H_4]$. Experimental results obtained through Algorithm 1 are presented in next section.

3. EXPERIMENTAL RESULTS

We test our method using a real airborne hyperspectral image (Fig. 1 (a)) with a HySpex VNIR sensor [18, 19] and the digital surface model (DSM) (Fig. 1 (c)) generated from image pairs acquired with the 4K camera system [15]. Both datasets were acquired at the same time over Oberpfaffenhofen, Bavaria, Germany between 8:42 and 8:56 a.m. (Central European Summer Time (CEST)) on June 4th, 2018. The

---

Algorithm 1: ADMM for the optimization problem in (9)

Input : E, F, X, e_N,λ,k_1,k_2,k_3
Output: A, Q, K
Initialize: $t = 0$,$A^{(0)}$, $Q^{(0)}$, $K^{(0)}$,$G^{(0)}$,$H^{(0)}$,$U^{(0)}$

1 **while** *the stopping criterion is not satisfied* **do**
2   Update $A^{(t+1)}$, given $Q^{(t)}$, $K^{(t)}$,$G^{(t)}$,$U^{(t)}$
3   Update $G^{(t+1)}$, given $A^{(t+1)}$, $U^{(t)}$
4   Update $Q^{(t+1)}$ and $K^{(t+1)}$, given $A^{(t+1)}$, $H^{(t)}$, $U^{(t)}$
5   Update $H^{(t+1)}$, given $Q^{(t+1)}$, $K^{(t+1)}$, $U^{(t)}$
6   Update $U^{(t+1)}$, given $U^{(t)}$, $A^{(t+1)}$, $Q^{(t+1)}$,$K^{(t+1)}$,$G^{(t+1)}$,$H^{(t+1)}$
7   t = t + 1
8 **end**

---

hyperspectral image has been atmospherically corrected using ATCOR [20]. After removing water vapor bands, a total of 101 bands have been kept for further processing. The DSM data are generated using the method in [15], followed by geometrically co-registration and re-sampling, in order to keep the same geo-coordinates and spatial resolution (i.e., 0.7 m) as the hyperspectral imagery. A spectral library of endmembers is generated by manually selecting pure pixels of relevant materials in sunlit regions of the image (Fig. 1 (b)). In addition, the sky view factor F is computed from the DSM data using the software SAGA GIS [16] (see Fig. 1 (d)). Given the F values, ten pairs of pixels have been selected in the scene in order to compute parameters k_1, k_2, and k_3 according to Eq. (1). Assuming that the atmospheric conditions are constant in the entire region, these parameters are assumed to be constant, and were set as: $k_1 = 0.5501$; $k_2 = 7.1303$; $k_3 = 0.1907$.

Fig. 2 compares the results of the proposed spectral mixing model in Eq. ((2)) with different constraints. Results in the first row consider the spectral and spatial constraints following Eqs. (5), (6), and (7), while results in the second row consider solely the spectral constraints of Eq. (5). For simplicity, we show two aggregate abundance maps of endmembers by grouping materials with similar spectra, resulting in the abundance maps of impervious surfaces (Fig. 2 (a) and (f)) and vegetation (Fig. 2 (b) and (g)). After embedding the spatial information, the abundance maps display better spatial relationships among pixels with a largely reduced noise level. Figs. 2 (d) and (i) compare the Q maps. Despite the fact that the proposed method does not enforce any spatial constraints on Q, the Q map in Fig. 2 (d) appears smoother while preserving small shadowed regions, thanks to the spatial constraints on the abundance maps. Following our previous works, the restored images in Fig. 2 (c) and (h) are computed by image reconstruction using the spectral mixing model in Eq. ((2)) with $Q = 0$. As the proposed method pro-
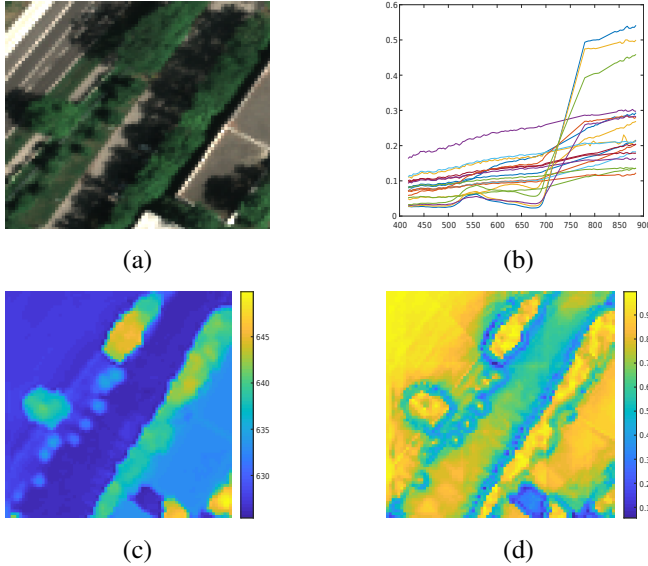
(a)

(b)

(c)

(d)

Fig. 1. Input data and computation of input parameters: (a) hyperspectral image as a true color composite acquired by the HySpex sensor in the study area of Oberpfaffenhofen, Bavaria, Germany; (b) endmember library, manually selected from (a); (c) DSM data and (d) F computed from the DSM data.

duces spatially smooth abundance maps and parameter maps, the reconstructed shadow-removed image (Fig. 2 (c)) is also spatially smooth.

4. CONCLUSION

This paper proposes a nonlinear spectral unmixing method by considering shadow and spatial relationships between neighboring pixels. We consider two illumination sources to improve the modeling of the spectra of shadowed pixels. In addition, we use image-generated DSM data to provide geometric information and promote the spatial relationships during the estimation of the abundances. We applied the proposed method to real airborne hyperspectral imagery. Experimental results demonstrate that the image-generated DSM offers great assistance in the proposed shadow-aware spectral mixing model. Firstly, the sky view factor feeds geometric information into the proposed spectral mixing model. Moreover, in shadowed regions where the spectra contain wavelength-dependent distortions, the height data assist in generating spatial relationships in the local neighborhood through weighting factors. By embedding the spatial relationships, the proposed method generates smoother abundance maps, parameter maps, and shadow-removed imagery.

5. REFERENCES

[1] Nicolas Dobigeon, Jean-Yves Tourneret, Cédric Richard, José Carlos M Bermudez, Stephen McLaughlin, and Alfred O Hero, "Nonlinear unmixing of hyperspectral images: Models and algorithms," *IEEE Signal processing magazine*, vol. 31, no. 1, pp. 82–94, 2013.

[2] José M Bioucas-Dias, Antonio Plaza, Nicolas Dobigeon, Mario Parente, Qian Du, Paul Gader, and Jocelyn Chanussot, "Hyperspectral unmixing overview: Geometrical, statistical, and sparse regression-based approaches," *IEEE journal of selected topics in applied earth observations and remote sensing*, vol. 5, no. 2, pp. 354–379, 2012.

[3] Rob Heylen, Mario Parente, and Paul Gader, "A review of nonlinear hyperspectral unmixing methods," *IEEE Journal of Selected Topics in Applied Earth Observations and Remote Sensing*, vol. 7, no. 6, pp. 1844–1868, 2014.

[4] Rob Heylen and Paul Scheunders, "A multilinear mixing model for nonlinear spectral unmixing," *IEEE transactions on geoscience and remote sensing*, vol. 54, no. 1, pp. 240–251, 2015.

[5] Andrea Marinoni and Paolo Gamba, "A novel approach for efficient p-linear hyperspectral unmixing," *IEEE Journal of Selected Topics in Signal Processing*, vol. 9, no. 6, pp. 1156–1168, 2015.

[6] Antonio Plaza, Pablo Martínez, Rosa Pérez, and Javier Plaza, "A quantitative and comparative analysis of endmember extraction algorithms from hyperspectral data," *IEEE transactions on geoscience and remote sensing*, vol. 42, no. 3, pp. 650–663, 2004.

[7] Rob Heylen, Vera Andrejchenko, Zohreh Zahiri, Mario Parente, and Paul Scheunders, "Nonlinear hyperspectral unmixing with graphical models," *IEEE Transactions on Geoscience and Remote Sensing*, vol. 57, no. 7, pp. 4844–4856, 2019.

[8] Guichen Zhang, Daniele Cerra, and Rupert Müller, "Shadow detection and restoration for hyperspectral images based on nonlinear spectral unmixing," *Remote Sensing*, vol. 12, no. 23, pp. 3985, 2020.

[9] Tatsumi Uezato, Naoto Yokoya, and Wei He, "Illumination invariant hyperspectral image unmixing based on a digital surface model," *IEEE Transactions on Image Processing*, vol. 29, pp. 3652–3664, 2020.

[10] Chen Shi and Le Wang, "Incorporating spatial information in spectral unmixing: A review," *Remote Sensing of Environment*, vol. 149, pp. 70–87, 2014.
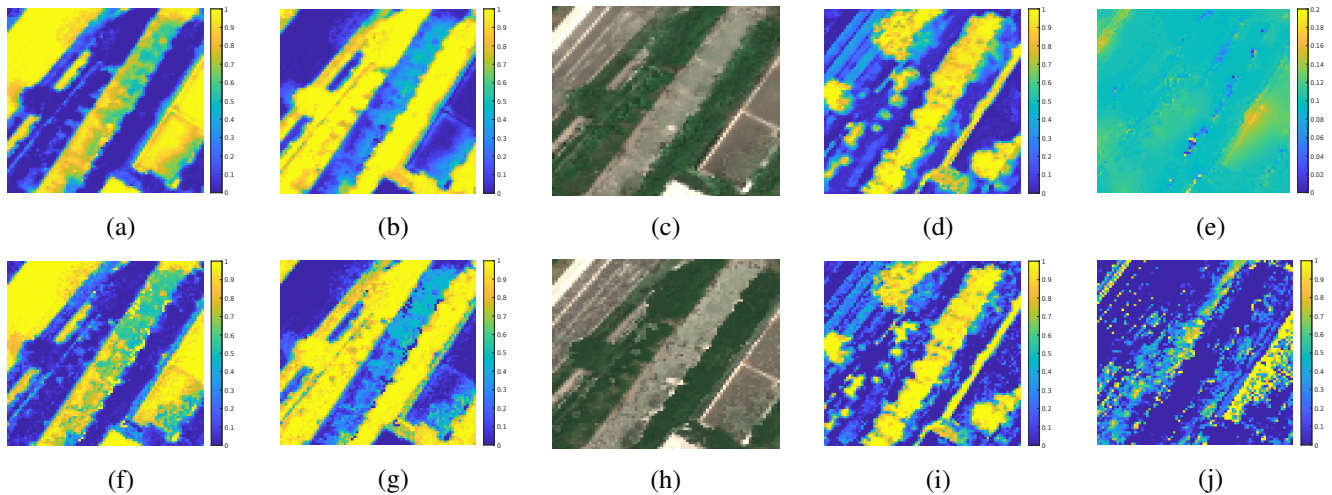
Fig. 2. First row: proposed model with spatial regularization; second row: model in Eq. ((2)) without spatial regularization. Columns: sum of abundances of impervious materials; sum of abundances of vegetation; shadow-removed images in true color composites; parameter Q; parameter K.

[11] Marian-Daniel Iordache, José M Bioucas-Dias, and Antonio Plaza, "Total variation spatial regularization for sparse hyperspectral unmixing," *IEEE Transactions on Geoscience and Remote Sensing*, vol. 50, no. 11, pp. 4484–4502, 2012.

[12] Junmin Liu, Jiangshe Zhang, Yuelin Gao, Chunxia Zhang, and Zhihua Li, "Enhancing spectral unmixing by local neighborhood weights," *IEEE Journal of Selected Topics in Applied Earth Observations and Remote Sensing*, vol. 5, no. 5, pp. 1545–1552, 2012.

[13] Tatsumi Uezato, Mathieu Fauvel, and Nicolas Dobigeon, "Hyperspectral image unmixing with lidar data-aided spatial regularization," *IEEE Transactions on Geoscience and Remote Sensing*, vol. 56, no. 7, pp. 4098–4108, 2018.

[14] Stephen Boyd, Neal Parikh, Eric Chu, Borja Peleato, Jonathan Eckstein, et al., "Distributed optimization and statistical learning via the alternating direction method of multipliers," *Foundations and Trends® in Machine learning*, vol. 3, no. 1, pp. 1–122, 2011.

[15] P d'Angelo and F Kurz, "Aircraft based real time bundle adjustment and digital surface model generation," *The International Archives of Photogrammetry, Remote Sensing and Spatial Information Sciences*, vol. 42, pp. 1643–1647, 2019.

[16] Olaf Conrad, Benjamin Bechtel, Michael Bock, Helge Dietrich, Elke Fischer, Lars Gerlitz, Jan Wehberg, Volker Wichmann, and Jürgen Böhner, "System for automated geoscientific analyses (saga) v. 2.1. 4," *Geo-scientific Model Development*, vol. 8, no. 7, pp. 1991–2007, 2015.

[17] Bin Yang and Bin Wang, "Band-wise nonlinear unmixing for hyperspectral imagery using an extended multilinear mixing model," *IEEE Transactions on Geoscience and Remote Sensing*, vol. 56, no. 11, pp. 6747–6762, 2018.

[18] Daniele Cerra, Miguel Pato, Kevin Alonso, Claas Köhler, Mathias Schneider, Raquel de los Reyes, Emiliano Carmona, Rudolf Richter, Franz Kurz, Peter Reinartz, et al., "Dlr hysu—a benchmark dataset for spectral unmixing," *Remote Sensing*, vol. 13, no. 13, pp. 2559, 2021.

[19] Claas Henning Köhler, "Airborne imaging spectrometer hyspex," *Journal of large-scale research facilities JLSRF*, vol. 2, no. A93, pp. 1–6, 2016.

[20] R Richter and D Schläpfer, "Atmospheric/topographic correction for airborne imagery," *ATCOR-4 user guide*, pp. 565–02, 2011.